Volume 12
Number 10
14 March 2021
Pages 3363–3790

Chemical Science

rsc.li/chemical-science

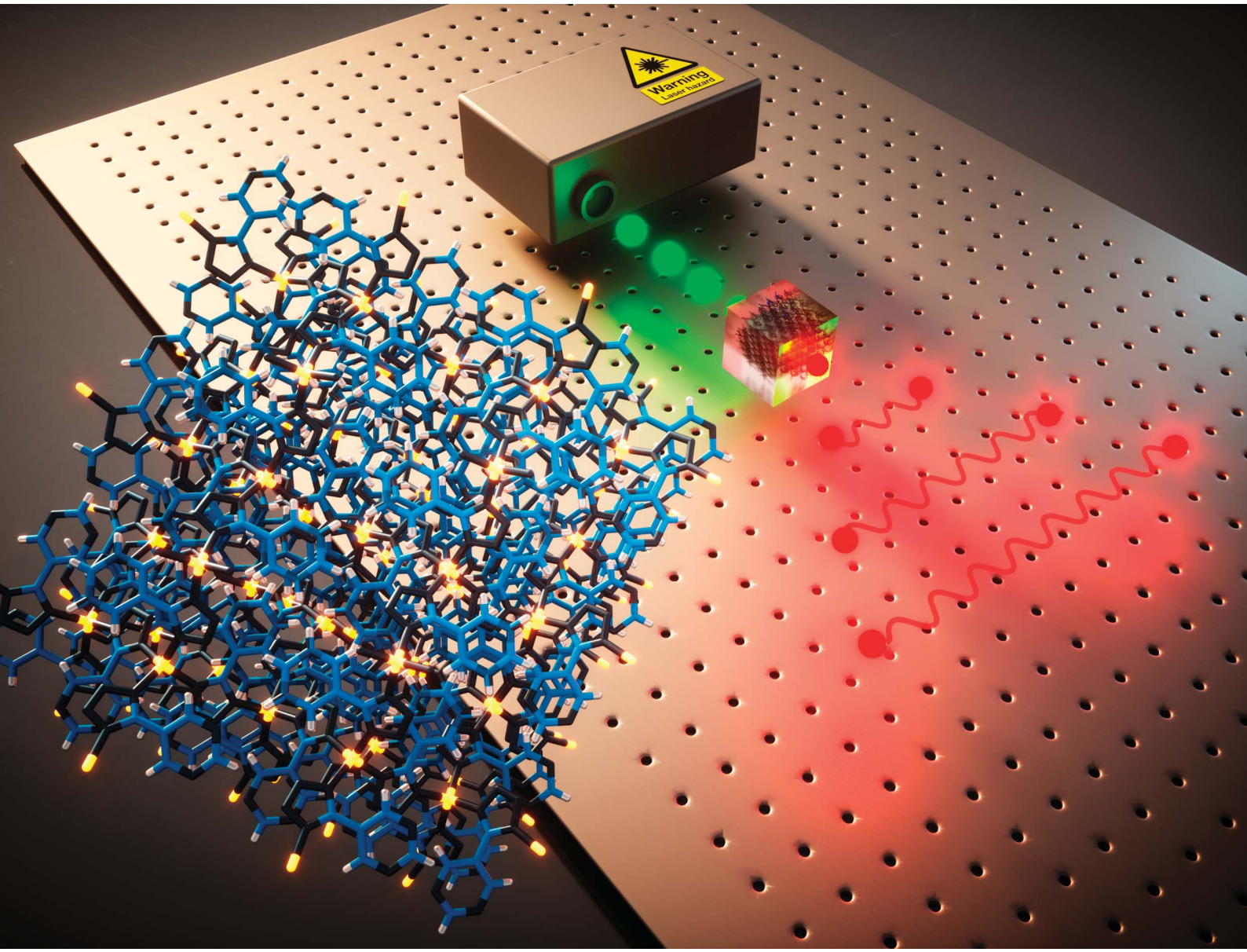

ISSN 2041-6539

ROYAL SOCIETY OF CHEMISTRY

EDGE ARTICLE
Felipe Herrera *et al.*
Engineering entangled photon pairs with metal–organic frameworks

Chemical Science

ROYAL SOCIETY OF CHEMISTRY

EDGE ARTICLE

View Article Online
View Journal | View Issue

Cite this: *Chem. Sci.*, 2021, **12**, 3475

All publication charges for this article have been paid for by the Royal Society of Chemistry

Received 4th October 2020
Accepted 19th January 2021

DOI: 10.1039/d0sc05572g

rsc.li/chemical-science

Engineering entangled photon pairs with metal–organic frameworks†

Rubén A. Fritz, [a] Yamil J. Colón [b] and Felipe Herrera *[ac]

The discovery and design of new materials with competitive optical frequency conversion efficiencies can accelerate the development of scalable photonic quantum technologies. Metal–organic framework (MOF) crystals without inversion symmetry have shown potential for these applications, given their nonlinear optical properties and the combinatorial number of possibilities for MOF self-assembly. In order to accelerate the discovery of MOF materials for quantum optical technologies, scalable computational assessment tools are needed. We develop a multi-scale methodology to study the wavefunction of entangled photon pairs generated by selected non-centrosymmetric MOF crystals *via* spontaneous parametric down-conversion (SPDC). Starting from an optimized crystal structure, we predict the shape of the $G^{(2)}$ intensity correlation function for coincidence detection of the entangled pairs, produced under conditions of collinear type-I phase matching. The effective nonlinearities and photon pair correlation times obtained are comparable to those available with inorganic crystal standards. Our work thus provides fundamental insights into the structure–property relationships for entangled photon generation with metal–organic frameworks, paving the way for the automated discovery of molecular materials for optical quantum technology.

I. Introduction

Optical communication and information technology that exploit the quantum properties of light for enhanced performance,[1] has enabled the development of quantum-secure communication networks,[2,3] fault-tolerant quantum computing,[4] and quantum sensing devices.[5] In quantum-enhanced applications, the theoretical performance limits can often be related to the quality of the underlying materials used in the implementation of a target protocol. The challenge for materials science is thus being able to tailor the conventional device development workflow such that the performance limits of specific quantum-enhanced protocols can be improved. For example, in several device-independent quantum key distribution protocols, the secure bit rate can be directly related to the flux of entangled photon pairs that can be generated in a nonlinear optical crystal subject to laser driving,[6,7] given a detection efficiency. The generation of entangled photon pairs *via* down-frequency conversion can in turn be mapped directly into a search for highly crystalline birefringent materials with large second-order nonlinearities, which can be used as entangled photon sources with high brightness.[8]

Optical quantum technologies have growing applications in enhanced imaging,[9] secure communication,[10] and quantum computing.[11] However, the prospects for expanding the reach of quantum-enhanced optical devices is limited, as the number of optical materials that are suitable for advanced protocols is relatively small.[12] For instance, inorganic crystals such as BaB_2O_4 (BBO) or KH_2PO_4 (KDP) are widely used for classical and quantum frequency conversion *via* three-wave mixing.[13] The optical anisotropy and large second-order nonlinear susceptibility of these materials in the visible and near infrared are exploited for spontaneous parametric down-conversion (SPDC),[14] a quantum optical process in which a single pump photon at frequency ω splits into two indistinguishable photons at $\omega/2$. The indistinguishability of the down-converted photons leads to entanglement of their degrees of freedom.[8] Despite their widespread use in practical quantum communication,[15] the Poissonian photon number distribution of the pump laser makes the SPDC photon pair generation events intrinsically probabilistic.[8] Deterministic (on-demand) generation of entangled photon pairs can be produced *via* the cascaded radiative decay of biexcitons in inorganic semiconductors,[16,17] cascaded decay of dipole-coupled emitters,[18] or by a combination of cascaded SPDC sources with conditional measurement events (heralding).[19] Regardless of their physical origin, photon pairs that are entangled in frequency,[8] polarization,[20] or spatial mode

[a]*Department of Physics, Universidad de Santiago de Chile, Av. Ecuador 3493, Santiago, Chile. E-mail: felipe.herrera.u@usach.cl*

[b]*Department of Chemical and Biomolecular Engineering, University of Notre Dame, IN, USA*

[c]*ANID – Millennium Science Initiative Program, Millennium Institute for Research in Optics, Chile*

† Electronic supplementary information (ESI) available. See DOI: 10.1039/d0sc05572g

profile,[21] are the building blocks of several quantum imaging and secure communication protocols.[22]

Inorganic crystals, in general, are considered to be robust materials. Zeolites are an example; they can be used in catalysis applications, usually at high temperatures.[23] Organic crystals are less stable but can provide great flexibility through molecular interactions and can be used as functional materials in drug delivery, catalysis, photonics, and electronics, and other applications.[24] Metal–organic frameworks (MOFs) are hybrid materials that combine the structural stability of inorganic crystals and the versatility of organic materials.[25] MOF crystals are very promising for applications in nonlinear optics.[12,14,26,27] Recent experimental reports of competitive second-order[28–30] and third-order optical nonlinearities[31] with polycrystalline MOF crystals, have stimulated the need to develop a computational methodology that is capable of screening the available MOF databases, and generate a list of leading candidate structures with a suitable combination of features in their linear and nonlinear optical responses that make them competitive materials for applications in quantum optics. Large-scale computational MOF screening methods for applications in gas storage and gas separation have been developed,[32,33] but extensions of these techniques are needed to discover novel applications of MOF materials in quantum technology.

In this work, we focus on selected non-centrosymmetric MOF crystals assembled from d^{10} transition metal ions (*e.g.*, Zn^{2+}, Cd^{2+}) as metal nodes, and pyridil-tetrazole (ptz) molecules as organic linkers. Due to the closed d-shell of the metal node, and the high HOMO–LUMO gap of the pyridil-tetrazole ligands,[34,35] the MOF crystals that we study are transparent throughout the visible spectrum up to the mid-infrared regime. For the MOF structures considered, the lack of inversion symmetry of their unit cells has enabled the observation of second-order nonlinear frequency conversion in polycrystalline powder samples with particle size in the range of microns.[26] Given the availability of low-cost optical testing techniques,[36] experiments have so far focused on the second-harmonic generation (SHG) process $\omega \rightarrow 2\omega$ from near-infrared to visible frequencies.[26] The reverse frequency conversion process $2\omega \rightarrow \omega$ corresponds to SPDC, which has yet to be demonstrated experimentally with MOFs. SPDC and SHG are conjugate processes in nonlinear optics.[13] Although their experimental implementation is different, the frequency conversion efficiencies of SHG and SPDC in a given crystal are determined by the same components of the nonlinear susceptibility tensor.[8] Therefore, understanding the material factors that determine SHG efficiencies is also relevant for future SPDC experiments.

In Fig. 1, we illustrate the qualitative behavior of the SHG signal intensity (I_{SHG}) at frequency 2ω upon illumination with a strong laser at frequency ω of a polycrystalline slab of non-centrosymmetric particles with propagation length L (panel a), and a single non-centrosymmetric crystal of equivalent propagation dimensions (panel b). For a powder sample, propagating optical waves sample an entire distribution of crystal orientations, defined by the direction of the optical axis of individual crystallites relative to the propagation light direction. This is the typical condition in SHG tests carried out with MOFs.[26] In this

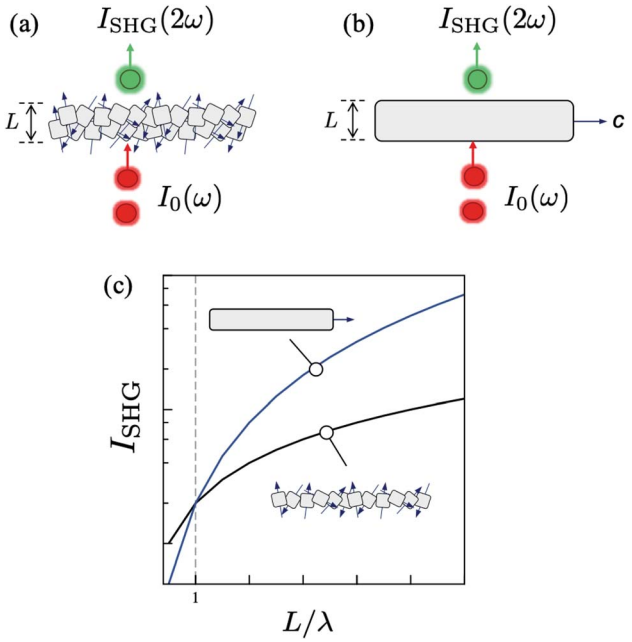

Fig. 1 Second harmonic generation (SHG) process $\omega \rightarrow 2\omega$ with a nonlinear crystal slab. (a) Polycrystalline slab with propagation length L composed by an ensemble of randomly oriented crystal particles. (b) Single crystal slab with well-defined orientation of the optical c-axis. (c) SHG intensity (log scale) as a function of the propagation length L (in units of pump wavelength λ), for polycrystalline and single-crystal slabs.

case, the SHG intensity scales linearly with L.[36,37] For crystals that support conditions of perfect phase matching (PPM),[13] this linear L-scaling is a suboptimal consequence of the random crystal orientation in the medium. In contrast, for a single crystal with same length L, the SHG intensity scales as L^2. In other words, the same nonlinear material at the same operating wavelengths has a superior output brightness in a second-order optical process when used as a single crystal. The phase coherence of the waves involved is also superior in single crystals. Fig. 1c shows that is not a critical issue for imaging and spectroscopy applications based on second-harmonic generation, which are typically used to study monolayers and interfaces with thickness L much smaller than the laser pump wavelength λ.[38,39] This quadratic scaling is beneficial for quantum nonlinear optical processes, such as SPDC, for two main reasons: (i) to maximize the brightness of the non-classical signal (number of entangled photon pairs) and; (ii) to optimize the degree of temporal correlations in coincidence detection (photon indistinguishability), which leads to the entanglement of photonic degrees of freedom.[40] None of these can be achieved using randomly oriented nonlinear crystal powders.

Growing large single crystal MOFs with millimeter dimensions is an experimental challenge. Few groups have reported large centrosymmetric crystals for applications in solid-phase chromatography.[41,42] As crystal engineering techniques for MOFs continue to improve,[43] we present here the first multi-scale computational design methodology for assessing the

entanglement properties of near-infrared entangled photon pairs produced *via* SPDC in a large non-centrosymmetric single crystal MOF under strong laser pumping. We carry out a detailed analysis of three transparent, non-centrosymmetric, birefringent MOFs having the same ptz ligand in their structure: $Zn(3\text{-ptz})_2$ (MIRO-101, CSD: 184958), $[Zn(H_2O)_6]NO_32(3\text{-ptz})$ (MIRO-102, CSD: 184132) and $CdN_3(3\text{-ptz})_2$ (MIRO-103, CSD: 184133). Efforts to grow high-quality single crystals of these MOF species for applications in optics are currently underway.[34,35]

II. Results

(A) Methodological overview

Starting from its optimized crystal structure, we compute the two-time intensity correlation function $G^{(2)}(\tau)$ for coincidence detection of entangled photon pairs generated *via* SPDC by a non-centrosymmetric MOF subject to strong laser pumping. The multi-scale calculation procedure we propose to achieve this, is described in detail in the ESI.† Briefly, we use solid-state DFT within the Coupled Perturbed Hartree–Fock/Kohn–Sham method (CPHF/KS)[44–46] with a PBE functional, to compute the band gap E_G, dynamical dielectric tensor $\varepsilon_{ij}(\omega)$, and dynamical second-order susceptibility tensor $\chi_{ijk}^{(2)}(\omega)$ of a fully optimized MOF crystal structure with non-centrosymmetric unit cell. Lattice disorder models are not implemented. Static disorder due to freely rotating organic groups is corrected from the experimental crystal structures, when needed. All DFT calculations were carried out using the CRYSTAL17 package.[47] The Sellmeier equations for ordinary and extraordinary crystal axes are obtained from $\varepsilon_{ij}(\omega)$, over a frequency range from the near infrared up to the crystal band gap. These are used to establish conditions for perfect phase matching in collinear type-I SPDC,[8] with signal output at 1064 nm. The effective nonlinearity d_{eff} is obtained by contracting the $\chi^{(2)}$ tensor with the appropriate input and output field polarizations. d_{eff} is used to parametrize an effective Hamiltonian for the SPDC process. The number of entangled photon pairs produced by the MOF, as well as the temporal and spectral properties of the entangled pair wavefunction can be computed from the effective Hamiltonian in first order perturbation theory. The $G^{(2)}$ function is fully determined by the photon pair wavefunction and the coincidence detection bandwidth.

(B) Phase matching conditions

The predicted band gaps E_G for the MOFs studied in this work are given in Table 1. The predicted band gap for MIRO 101 agrees well with recent experiments.[48] We also compute the band gap of IRMOF-1, to compare with experiments and previous calculations in the literature.[49–51] For IRMOF-1, the PBE-GGA functional is found to be in better agreement with experiments than the B3LYP-D calculations used in ref. 52, which overestimate the band gap. As mentioned above, the PBE-GGA functional is used for MIRO-101, MIRO-102, and MIRO-103. As additional validation of our methods, we also compute the band gaps of β-barium borate (BBO) and potassium dihydrogen phosphate (KDP), two widely used inorganic nonlinear crystals. The results are in good agreement with measured band gaps, although further basis set optimization may be needed for KDP.

Table 1 Calculated [calc] and measured [exp] band gaps E_G for MIRO-101, MIRO-102, and MIRO-103 single crystals. Values for IrMOF-1, β-barium borate (BBO) and potassium dihydrogen phosphate (KDP) are shown for comparison

	E_G (eV) [calc]	E_G (eV) [exp]
MIRO-101	3.15	3.32 (ref. 48)
MIRO-102	3.10	—
MIRO-103	2.98	—
IRMOF-1	3.62	3.4–4.0 (ref. 49–51)
BBO	6.18	6.43 (ref. 53)
KDP	5.90	7.12 (ref. 54)

In Fig. 2, we show the unit cell structures and the Sellmeier curves $n^2(\lambda)$ of our target MOFs. We obtain these from the dielectric tensor $\varepsilon_{ij}(\omega)$, computed at regular wavelength intervals from $\lambda_{\min} = hc/E_G$ to $\lambda_{\max} = 1100$ nm. For the phase-matching geometry considered below, we are interested in the Sellmeier curves along the ordinary axis (n_o) and the extraordinary *c*-axis (n_e). For each crystal axis, we fit the *ab initio* curves to the standard relation

$$n^2(\lambda) = A + \frac{B\lambda^2}{\lambda^2 - C} + \frac{B_1\lambda^2}{\lambda^2 - C_1}. \quad (1)$$

The fitted Sellmeier coefficients for each MOF are given in the ESI.† MIRO-101 is negative uniaxial ($n_e < n_o$), MIRO-103 is positive uniaxial ($n_e > n_o$). Although MIRO-102 is biaxial, one can always fix the crystal orientation such that light propagation is influenced by two refractive indices only.[55] We aim for obtaining accurate values for the dynamic birefringence $\Delta n(\omega) \equiv n_e(\omega) - n_o(\omega)$ through the frequency range of interest, as this is the observable that most strongly determines the phase matching conditions in SPDC. The phase matching conditions are invariant with respect to an overall change of the static average refractive index $\bar{n} = [n_e(\lambda) + n_o(\lambda)]/2$ for $\lambda \to \infty$. In other words, we can vertically shift all the Sellmeier curves in Fig. 2 by a constant value, and the phase matching results discussed below would not be affected.

SPDC is a three-wave mixing process in which photons from a strong pump laser field at frequency ω_p are coherently converted into a pair of signal photons with frequencies ω_1 and ω_2 such that $\omega_p = \omega_1 + \omega_2$,[8] as expected for a perturbative light–matter interaction process that conserves energy. In the photon conversion process, conservation of momentum leads to the condition for perfect phase matching $\mathbf{k}_p = \mathbf{k}_1 + \mathbf{k}_2$, where $\mathbf{k}$ is a wavevector. In general, phase matching is a vectorial condition that together with energy conservation determines the propagation directions and frequencies of the photons generated in an entangled pair. Several possibilities can be analyzed, depending on the polarizations and propagation directions of

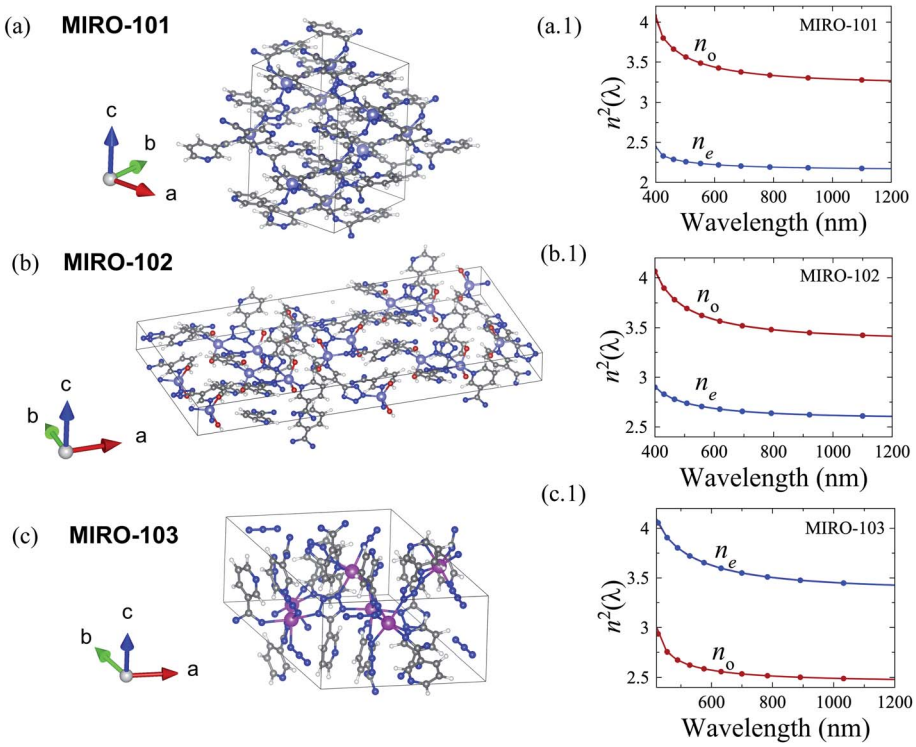

Fig. 2 MOF structures and *ab initio* Sellmeier curves. (a) Unit cell for $Zn(3\text{-ptz})_2$ (MIRO-101), (b) $[Zn(H_2O)_6]NO_3\text{-}2(3\text{-ptz})$ (MIRO-102), (c) $CdN_3(3\text{-ptz})_2$ (MIRO-103). Color code displays hydrogen atoms (white), carbon (gray), nitrogen (blue) and zinc (violet). The corresponding Sellmeier curves for the extraordinary (n_e) and ordinary axes (n_o) of each crystal structure, are shown to the right of each structure.

interest in experiments.[56] We consider collinear phase matching, in which the pump and signal photons share the same propagation direction **k**. The perfect phase matching condition thus reduces to a scalar relation for the refractive indices given by $\omega_p n_p(\omega_p) = \omega_1 n_1(\omega_1) + \omega_2 n_2(\omega_2)$, where n_p is the refractive index of the pump wave, n_1 and n_2 are the refractive indices of the signal photons. We assume that the detected signal photons are degenerate ($\omega_1 = \omega_2 = \omega_p/2$), thus reducing the condition to $n_p(\omega_p) = n_s(\omega_p/2)$, where $n_s(\omega)$ denotes the refractive index of the signal photons. An additional ambiguity remains regarding the polarizations of the pump and signal waves. For the negative uniaxial MIRO-101 and MIRO-103 crystals, we adopt conventional *oee* type-I conditions,[13] where the entangled signal photons are polarized along the ordinary axis (o), and the pump is polarized along the extraordinary axis (e). For MIRO-102, *eoo* type-I conditions are used. We focus on degenerate collinear signal photons to simplify the phase matching analysis. Non-degenerate and non-collinear conditions are also possible.[8]

In a collinear configuration, the common propagation vector **k** of the pump and signal waves has a polar angle θ relative to the optical c-axis and azimuthal angle ϕ with respect to the X-axis, as show in Fig. 3a. Consider now that the waves propagate

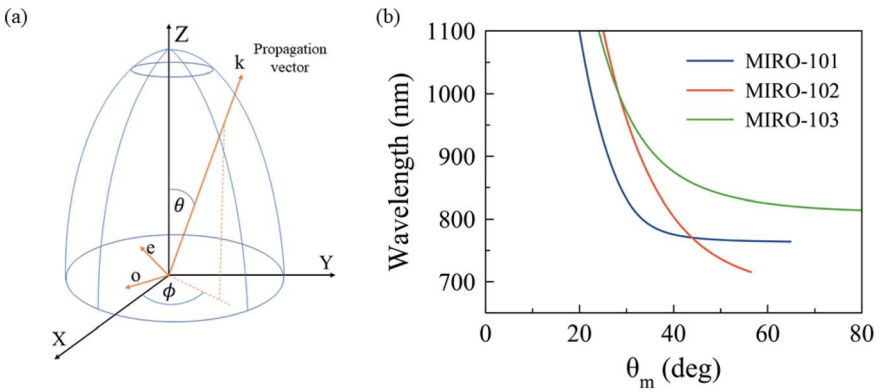

Fig. 3 Type-I phase matching for entangled photon pair generation. (a) For a pump field at frequency ω, wavevector **k** and polarization vector $\mathbf{e}_o$ along the ordinary axis, an entangled photon pair is produced *via* SPDC with an extraordinary polarization $\mathbf{e}_e$. In the collinear scenario, all waves propagate at an angle θ relative to the optical axis of the crystal (Z-direction). We set the azimuthal angle to $\phi = \pi/2$. (b) Perfect phase matching angle θ_m for MIRO-101, MIRO 102, and MIRO-103 for a range of signal wavelengths.

along the X-axis ($\theta = \phi = \pi/2$). Signal photons thus have extraordinary polarization along Z, and the perfect phase matching condition reads $n_o(\omega_p) = n_e(\omega_p/2)$. From the Sellmeier curves in Fig. 2, we see that this condition cannot be satisfied for any choice of ω_p in the visible spectrum. This is common for materials with large birefringence.[13] Perfect phase matching in our uniaxial MOF crystals can still be achieved if the pump and signal waves have propagation components along both ordinary and extraordinary directions. In Fig. 3b, we plot the predicted angle of perfect phase matching θ_m for MIRO-101, MIRO-102, and MIRO-103, over a range of entangled photon wavelengths λ_s in the near infrared. We set $\phi = \pi/2$ here for concreteness, but below this constraint is relaxed when we discuss effective nonlinearities.

(C) Entangled photon pair properties

In Fig. 4, we illustrate collinear type-I spontaneous parametric down-conversion (SPDC) in a nonlinear MOF crystal, for the generation of entangled photon pairs in the near infrared. Pump photons from a strong visible laser field are coherently converted into photon pairs described by a wavefunction of the form

$$|\Psi_2\rangle = \lambda L \int \mathrm{d}k_1 \int \mathrm{d}k_2 Q(k_1, k_2) \hat{a}^\dagger_{k_1} \hat{a}^\dagger_{k_2} |0\rangle_1 |0\rangle_2, \quad (2)$$

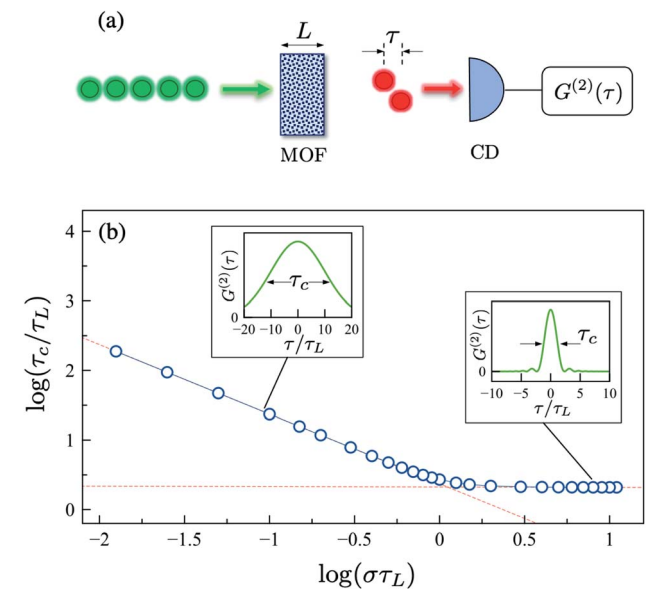

Fig. 4 Entangled photon pair generation with metal–organic frameworks. (a) Visible photons (green circles) are pumped into a non-centrosymmetric MOF single crystal with propagation length L. Entangled photon pairs at half the pump frequency (red circles), emerge from the crystal with a small delay τ. Each pair is collected with a coincidence detector (CD), and the delay times are post-processed to give a two-time correlation function $G^{(2)}(\tau)$. (b) Log–log plot of the correlation time τ_c (FWHM) as a function of detector bandwidth σ for collinear SPDC with type-I phase matching. Time is in units of $\tau_L = \sqrt{\beta_2 L/4}$. Representative $G^{(2)}$ functions in the narrowband and broadband regimes are shown for comparison. β_2 is the group velocity dispersion at the pair frequency.

where L is the crystal propagation and λ is an effective nonlinear coupling given by

$$\lambda = i \frac{2A_0 d_{\mathrm{eff}}}{\hbar} \int \mathrm{d}^2\mathbf{r}_\perp A_p^*(\mathbf{r}_\perp) A_1(\mathbf{r}_\perp) A_2(\mathbf{r}_\perp), \quad (3)$$

where A_0 is the peak field amplitude of the pump laser field, $d_{\mathrm{eff}} = (\varepsilon_0/2)\chi_{ijk}^{(2)} e_i e_j e_k$ is the effective second-order nonlinearity obtained as a contraction of the $\chi^{(2)}$ tensor of the crystal and the field polarizations assumed in our phase matching configuration.[13] The spatial integral is the transverse mode overlap between the pump and signal fields. This quantity depends on the pump beam geometry and the crystal dimensions.

The photon pair (biphoton) wavefunction in eqn (2) is a non-separable wavepacket of the one-photon frequency-domain contributions $\hat{a}^\dagger_{k_j}|0\rangle_j$, for $j = 1, 2$. The spectral and temporal properties of the biphoton state are determined by the joint spectral function

$$Q(k_1, k_2) = l(\omega_1) l(\omega_2) \mathrm{sinc}(\Delta k L/2) \mathrm{e}^{i\Delta k L/2} \alpha_p(\omega_1 + \omega_2), \quad (4)$$

where $\Delta k \equiv k_p - k_1 - k_2$ is the phase mismatch, $\alpha_p(\omega)$ is the normalized pump spectral amplitude evaluated at ω_p, and $l(\omega_j)$ are slowly-varying functions in frequency. Generalizations of eqn (4) to account for linear losses are straightforward.[57] The derivation of eqn (2) closely follows ref. 8, and is reproduced in the ESI.†

The arrival times for all the photon pairs emitted by the MOF crystal are detected in a coincidence setup, as illustrated in Fig. 4a. The probability of detecting a photon at time t_1 and a second photon at time t_2 is proportional to the (unnormalized) intensity correlation function $G^{(2)}(t_1, t_2) = |\langle 0|\hat{E}^{(+)}(t_2)\hat{E}^{(+)}(t_1)|\Psi_2\rangle|^2$,[58] where the far-field operators $\hat{E}^{(+)}(t_j) = \int \mathrm{d}\omega f(\omega)\hat{a}(\omega)e_i\omega t_j$ take into account any spectral filtering done at the detectors through the filter function $f(\omega)$. For SPDC sources, the $G^{(2)}$ depends only on the relative time $\tau = t_1 - t_2$.[8] The actual number of entangled photon pairs produced by a MOF crystal (brightness) can be evaluated for perfect crystals from eqn (2) and (3), knowing the pump spectral profile, the transverse intensity profiles of the pump and signal fields, and the signal propagation length. For real crystals, the level of attenuation losses (in dB mm^{-1}) due to Fresnel reflection and light scattering, at the pump and signal frequencies, should also be known.[57] Technical details and crystal imperfections apart, the source brightness always scales as d_{eff}^2, the intrinsic MOF property that can be evaluated from first principles.

In addition to the number photon pairs produced in SPDC, another feature that is important in applications is the pair correlation time τ_c, a measure of how indistinguishable (*i.e.*, entangled) are two photons in a pair. τ_c can be defined as the width of the $G^{(2)}$ function. Pairs of distinguishable uncorrelated photons cannot be used in entanglement-based applications.[21] The width of the $G^{(2)}$ function not only depends on the intrinsic material properties of a MOF structure, such as its Sellmeier curves along the ordinary and extraordinary axes, but also on the details of the optical pump and detection setup.[8] Explicitly, for degenerate type-I phase matching, we can write the intensity correlation function as

$$G^{(2)}(\tau) \propto \left| \int \mathrm{d}\nu \ \mathrm{sinc}\left[(\beta_2 L/4)\nu^2\right] \mathrm{e}^{-\nu^2/\sigma^2} \mathrm{e}^{i\nu\tau} \right|^2, \quad (5)$$

Table 2 Calculated phase matching angle θ_m, d_{eff} evaluated at the propagation direction (θ_m, ϕ) in collinear type-I SPDC at 1064 nm, group velocity dispersion (GVD) at perfect phase matching for ordinary (o) and extraordinary (e) propagation directions, and the corresponding photon pair correlation times τ_c. Our calculated θ_m and d_{eff} for BBO and KDP are compared with experimental values from ref. 59. In all cases we set the crystal length to $L = 1.5$ mm

	θ_m (deg)	d_{eff} (pm V^{-1})	ϕ (deg)	GVD$_o$ (fs^2 mm^{-1})	GVD$_e$ (fs^2 mm^{-1})	τ_c^o (fs)	τ_c^e (fs)
MIRO-101	20.8	−0.35	80°	213.18	77.60	17.88	10.78
		+0.35	170°				
MIRO-102	26.1	+0.08	90°	204.47	114.12	17.51	13.08
MIRO-103	25.4	+0.12	0°	129.92	243.18	13.96	19.1
		−0.14	70°				
BBO (calc)	22.9	1.82	0°	38.01	37.11	7.55	7.46
BBO (exp)	22.8 (ref. 59)	2.11 (ref. 59)					
KDP (calc)	40.4	0.41	45°	−8.04	19.83	—	5.46
KDP (exp)	41 (ref. 59)	0.29 (ref. 59)					

where β_2 is the group velocity dispersion (GVD) of the degenerate signal photons and σ is the width of the spectral filter function $f(\omega)$, assumed here to be Gaussian without loss of generality. The integration over the frequency detuning ν accounts for all possible signal photons that do not satisfy perfect phase matching conditions $\Delta k = 0$, but still satisfy energy conservation. We neglect deviations from $\Delta k = 0$ beyond second order in ν. Photons in a pair with detuning much larger than the detector bandwidth do not contribute to the correlation function, even if they arrive at the same time ($\tau = 0$) at the detectors.

In Fig. 4, we plot the correlation time τ_c for type-I SPDC under collinear type-I phase matching as a function of the detector bandwidth σ (log–log scale). Time is in units of the characteristic crystal timescale $\tau_L = \sqrt{\beta_2 L/4}$, which roughly corresponds to the width of the sinc function in eqn (5). In the broadband detection limit ($\sigma \gg 1/\tau_L$), we have that $\tau_c \approx 2.0\tau_L$. Therefore, given a crystal length L, we can compute τ_c for a given MOF crystal by evaluating β_2 from the Sellmeier curve obtained from first principles. For concreteness, the GVD parameter for MIRO-101 under conditions of perfect phase matching at $\lambda =$ 1064 nm is estimated to be $\beta_2 = 77.60$ fs^2 mm^{-1}. For a crystal length $L = 1.5$ mm, the estimated correlation time is $\tau_c \approx 10.78$ fs for this MOF crystal. Fig. 4 shows that this broadband value only represents a lower bound for τ_c for this crystal, since the biphoton wavepacket is expected to broaden in time when a finite detector bandwidth is taken into account. For example, by using a spectral filters with a relatively broad linewidth $\sigma = 0.2/\tau_L \approx 15$ THz (FWHM), the coincidence correlation time now becomes $\tau_c \approx 155$ fs, for the same crystal parameters.

In Table 2, we summarize the results obtained for SPDC with collinear type-I phase matching for MIRO-101, MIRO-102, and MIRO-103 crystal slabs with length $L = 1.5$ mm. We obtain angles of perfect phase matching θ_m at 1064 nm, the effective nonlinearity d_{eff} at perfect phase matching, and the characteristic crystal timescales τ_L for ordinary and extraordinary signal field polarizations. For a given coincidence detection bandwidth σ, the photon pair correlation time τ_c can be estimated. As an additional validation of our DFT methods, we also compute the phase matching angle and GVD for BBO and KDP crystals, obtaining results that agree well with measurements at 1064 nm.[59] For BBO, the predicted photon pair correlation time ($\tau_c \approx 7.5$ fs) for a crystal length $L = 1.5$ mm with $\lambda_s = 1064$ nm degenerate signal and idler fields, should be compared with $\tau_c \approx 17$ fs, estimated from the width of the joint spectral function for signal photons produced by a 1 mm crystal at $\lambda_s = 808$ nm, under degenerate collinear type-I phase matching conditions.[60]

In general, we expect the MOF observables in Table 2 to have a dependence with temperature, since thermal lattice distortions are known to influence the response of optical crystals.[59,61,62] The *ab initio* analysis of the refractive index gradients $dn(\lambda)/dT$ is possible,[63] but falls outside the scope of this work. We can still estimate an upper bound on the expected temperature dependence of the Sellmeier curves for MIRO-101, MIRO-102 and MIRO-103, which share a dipolar push–pull organic ligand, from experiments on liquid crystals made of large dipolar aromatic molecules. Thermal molecular motions are arguably more significant in liquid crystals than in the nonporous MOFs studied here. For liquid crystals with commonly used dipolar chromophores, the index gradient at visible frequencies is on the order of 10^{-4} °C^{-1},[64–66] whereas for inorganic crystals we have $dn/dT \sim 10^{-6}$ °C^{-1}.[59] Therefore, we do not expect the Sellmeier curves in Fig. 2 to vary by more than 1% over 100 °C, a variation that is smaller than systematic DFT errors.

III. Conclusions

In this work, we develop multi-scale methodology for the computational characterization of quantum light generated by nonlinear metal–organic frameworks. Specifically, we study entangled photon pair generation in the near infrared *via* spontaneous parametric down conversion (SPDC) in three zinc-tetrazole MOF crystals with non-centrosymmetric and nonporous unit cells: Zn(3-ptz)$_2$ (MIRO-101), [Zn(H$_2$O)$_6$]NO$_3$2(3-ptz) (MIRO-102) and CdN$_3$(3-ptz)$_2$ (MIRO-103). Using solid-state DFT, we determine the band gaps and Sellmeier equations of these crystals. The MOFs studied are strongly birefringent, and allow conditions for type-I and type-II phase matching in SPDC. We focus on a collinear type-I scenario to illustrate the potential

of our method for understanding the temporal and frequency correlations of the entangled photon pair (biphoton) wavefunction produced under strong laser pumping of the MOF crystals. Other phase matching scenarios are straightforward extensions of our type-I analysis.

The similar band gaps (3.0–3.1 eV) and phase matching angles (21–26°) of the MOFs studied suggest that these properties largely depend on the molecular properties of the ligand (3-ptz). On the other hand, larger variations of the effective nonlinearities (d_{eff}) predicted under equal phase matching configuration, suggest a stronger sensibility on the crystal lattice geometry. However, only a large-scale analysis over an entire database of suitable nonlinear MOF structures would provide reliable structure–property relationships.

We have shown that MOF crystals can give entangled photon signals that are comparable with industry standards. However, the real untapped potential, thus importance, of using MOFs for quantum optical applications rests on the essentially unbounded design space for MOF self-assembly, given a library of suitable metal nodes and organic linkers.[32,33] The Cambridge Structural Database currently lists over 2000 non-centrosymmetric MOF structures with closed-shell Zn nodes without structural disorder, each with a published synthetic protocol. MIRO-101, MIRO-102, and MIRO-103 are a subset of the database. Therefore, as a material class, metal–organic frameworks are promising for non-linear quantum optics because they can be computationally screened on a large scale to satisfy a set of conditions needed for a desired quantum optical technique. As a result of the screening, we can discover specific MOF crystals that significantly outperform inorganic industry standard on a given application. Our work thus paves the way for the computational discovery of novel metal–organic framework materials that are favorable for target protocols in optical quantum technology.

Conflicts of interest

There are no conflicts to declare.

Acknowledgements

We thank Gustavo Lima and Stephen Walborn for comments. RAF is supported by DICYT-USACH grant POSTDOC 041831HU. FH thanks support from CONICYT through Proyecto REDES ETAPA INICIAL, Convocatoria 2017 no. REDI 170423, FONDECYT Regular No. 1181743. This work was funded by ANID – Millennium Science Initiative Program ICN17-012. YJC thanks the University of Notre Dame for financial support through start-up funds.

References

1 J. L. O'Brien, A. Furusawa and J. Vučković, *Nat. Photonics*, 2009, **3**, 687–695.
2 H. J. Kimble, *Nature*, 2008, **453**, 1023–1030.
3 S. Wehner, D. Elkouss and R. Hanson, *Science*, 2018, **362**(6412), eaam9288.
4 J. Wang, F. Sciarrino, A. Laing and M. G. Thompson, *Nat. Photonics*, 2020, **14**, 273–284.
5 S. Pirandola, B. R. Bardhan, T. Gehring, C. Weedbrook and S. Lloyd, *Nat. Photonics*, 2018, **12**, 724–733.
6 F. Xu, B. Qi, Z. Liao and H.-K. Lo, *Appl. Phys. Lett.*, 2013, **103**, 061101.
7 L. Masanes, S. Pironio and A. Acín, *Nat. Commun.*, 2011, **2**, 238.
8 Y. Shih, *Rep. Prog. Phys.*, 2003, **66**, 1009–1044.
9 Y. Shih, *IEEE J. Sel. Top. Quantum Electron.*, 2007, **13**, 1016–1030.
10 N. Gisin and R. Thew, *Nat. Photonics*, 2007, **1**, 165–171.
11 P. Kok, W. J. Munro, K. Nemoto, T. C. Ralph, J. P. Dowling and G. J. Milburn, *Rev. Mod. Phys.*, 2007, **79**, 135–174.
12 R. Medishetty, *Chem. Soc. Rev.*, 2017, **46**, 4976–5004.
13 R. W. Boyd, *Nonlinear Optics*, Elsevier, Burlington, MA USA, 3rd edn, 2008.
14 L. R. Mingabudinova, V. V. Vinogradov, V. A. Milichko, E. Hey-Hawkins and A. V. Vinogradov, *Chem. Soc. Rev.*, 2016, **45**, 5408–5431.
15 R. Bedington, J. M. Arrazola and A. Ling, *npj Quantum Inf.*, 2017, **3**, 30.
16 N. Akopian, N. H. Lindner, E. Poem, Y. Berlatzky, J. Avron, D. Gershoni, B. D. Gerardot and P. M. Petroff, *Phys. Rev. Lett.*, 2006, **96**, 130501.
17 A. Fognini, A. Ahmadi, M. Zeeshan, J. T. Fokkens, S. J. Gibson, N. Sherlekar, S. J. Daley, D. Dalacu, P. J. Poole, K. D. Jöns, V. Zwiller and M. E. Reimer, *ACS Photonics*, 2019, **6**, 1656–1663.
18 D. S. Wang, T. Neuman and P. Narang, *Dipole-Coupled Defect Pairs as Deterministic Entangled Photon Pair Sources*, 2020.
19 A. Dousse, J. Suffczyński, A. Beveratos, O. Krebs, A. Lemaître, I. Sagnes, J. Bloch, P. Voisin and P. Senellart, *Nature*, 2010, **466**, 217–220.
20 T. E. Kiess, Y. H. Shih, A. V. Sergienko and C. O. Alley, *Phys. Rev. Lett.*, 1993, **71**, 3893–3897.
21 L. Neves, G. Lima, J. G. Aguirre Gómez, C. H. Monken, C. Saavedra and S. Pádua, *Phys. Rev. Lett.*, 2005, **94**, 100501.
22 V. Scarani, H. Bechmann-Pasquinucci, N. J. Cerf, M. Dusek, N. Lutkenhaus and M. Peev, *Rev. Mod. Phys.*, 2009, **81**, 1301–1350.
23 N. Rahimi and R. Karimzadeh, *Appl. Catal., A*, 2011, **398**, 1–17.
24 J. S. Brooks, *Chem. Soc. Rev.*, 2010, **39**, 2667–2694.
25 H. Furukawa, K. E. Cordova, M. O'Keeffe and O. M. Yaghi, *Science*, 2013, **341**, 6149.
26 C. Wang, T. Zhang and W. Lin, *Chem. Rev.*, 2012, **112**, 1084–1104.
27 X. Yang, X. Lin, Y. S. Zhao and D. Yan, *Chem.–Eur. J.*, 2018, **24**(25), 6484–6493.
28 S. Van Cleuvenbergen, I. Stassen, E. Gobechiya, Y. Zhang, K. Markey, D. E. De Vos, C. Kirschhock, B. Champagne, T. Verbiest and M. A. van der Veen, *Chem. Mater.*, 2016, **28**, 3203–3209.
29 Y.-X. Zhang, B.-X. Li, H. Lin, Z. Ma, X.-T. Wu and Q.-L. Zhu, *J. Mater. Chem. C*, 2019, **7**, 6217–6221.

30 Z. Chen, G. Gallo, V. A. Sawant, T. Zhang, M. Zhu, L. Liang, A. Chanthapally, G. Bolla, H. S. Quah, X. Liu, K. P. Loh, R. E. Dinnebier, Q.-H. Xu and J. J. Vittal, *Angew. Chem., Int. Ed.*, 2020, **59**, 833–838.
31 M. Liu, H. S. Quah, S. Wen, Z. Yu, J. J. Vittal and W. Ji, *Chem. Mater.*, 2016, **28**, 3385–3390.
32 Y. J. Colón and R. Q. Snurr, *Chem. Soc. Rev.*, 2014, **43**, 5735–5749.
33 A. Sturluson, M. T. Huynh, A. R. Kaija, C. Laird, S. Yoon, F. Hou, Z. Feng, C. E. Wilmer, Y. J. Colón, Y. G. Chung, D. W. Siderius and C. M. Simon, *Mol. Simul.*, 2019, **45**, 1082–1121.
34 I. Chi-Durán, J. Enríquez, C. Manquian, K. Wrighton-Araneda, W. Cañon-Mancisidor, D. Venegas-Yazigi, F. Herrera and D. P. Singh, *ACS Omega*, 2018, **3**, 801–807.
35 J. Enríquez, C. Manquian, I. Chi-Duran, F. Herrera and D. P. Singh, *ACS Omega*, 2019, **4**, 7411–7419.
36 S. K. Kurtz and T. T. Perry, *J. Appl. Phys.*, 1968, **39**, 3798–3813.
37 I. Aramburu, J. Ortega, C. L. Folcia and J. Etxebarria, *Appl. Phys. B: Lasers Opt.*, 2014, **116**, 211–233.
38 T. F. Heinz, C. K. Chen, D. Ricard and Y. R. Shen, *Phys. Rev. Lett.*, 1982, **48**, 478–481.
39 L. Schneider and W. Peukert, *Part. Part. Syst. Charact.*, 2006, **23**, 351–359.
40 M. Fiorentino, S. M. Spillane, R. G. Beausoleil, T. D. Roberts, P. Battle and M. W. Munro, *Opt. Express*, 2007, **15**, 7479–7488.
41 S. Han, Y. Wei, C. Valente, I. Lagzi, J. J. Gassensmith, A. Coskun, J. F. Stoddart and B. A. Grzybowski, *J. Am. Chem. Soc.*, 2010, **132**, 16358–16361.
42 L. Li, F. Sun, J. Jia, T. Borjigin and G. Zhu, *CrystEngComm*, 2013, **15**, 4094–4098.
43 B. Seoane, S. Castellanos, A. Dikhtiarenko, F. Kapteijn and J. Gascon, *Coord. Chem. Rev.*, 2016, **307**, 147–187.
44 M. Ferrero, M. Rérat, R. Orlando and R. Dovesi, *J. Chem. Phys.*, 2008, **128**, 014110.
45 M. Ferrero, M. Rérat, R. Orlando and R. Dovesi, *J. Comput. Chem.*, 2008, **29**, 1450–1459.
46 M. Ferrero, M. Rérat, B. Kirtman and R. Dovesi, *J. Chem. Phys.*, 2008, **129**, 244110.
47 A. Erba, J. Baima, I. Bush, R. Orlando and R. Dovesi, *J. Chem. Theory Comput.*, 2017, **13**, 5019–5027.
48 I. Chi-Duran, R. Fritz, V. Olaya, R. Urzua-Leiva, G. I. Cárdenas-Jirón, D. P. Singh and F. Herrera, Anisotropic Band-Edge Absorption of Millimeter-Size Zn(3-Ptz)2 Single Crystal Metal-Organic Frameworks, 2020, DOI: 10.26434/chemrxiv.13370414.v1.
49 S. Bordiga, C. Lamberti, G. Ricchiardi, L. Regli, F. Bonino, A. Damin, K.-P. Lillerud, M. Bjorgen and A. Zecchina, *Chem. Commun.*, 2004, 2300–2301.
50 M. Alvaro, *et al.*, *Chem.–Eur. J.*, 2007, **13**, 5106–5112.
51 L.-M. Yang, P. Vajeeston, P. Ravindran, H. Fjellvag and M. Tilset, *Inorg. Chem.*, 2010, **49**, 10283–10290.
52 M. R. Ryder, L. Donà, J. G. Vitillo and B. Civalleri, *ChemPlusChem*, 2018, **83**, 308–316.
53 R. H. French, J. W. Ling, F. S. Ohuchi and C. T. Chen, *Phys. Rev. B: Condens. Matter Mater. Phys.*, 1991, **44**, 8496–8502.
54 V. Lacivita, M. Rérat, B. Kirtman, M. Ferrero, R. Orlando and R. Dovesi, *J. Chem. Phys.*, 2009, **131**, 204509.
55 R. E. Stoiber and S. A. Morse, in *Biaxial Crystal Optics*, Springer US, Boston, MA, 1994, pp. 159–171.
56 J. E. Midwinter and J. Warner, *Br. J. Appl. Phys.*, 1965, **16**, 1135–1142.
57 M. G. Moebius, F. Herrera, S. Griesse-Nascimento, O. Reshef, C. C. Evans, G. G. Guerreschi, A. Aspuru-Guzik and E. Mazur, *Opt. Express*, 2016, **24**, 9932–9954.
58 M. O. Scully and M. S. Zubairy, *Quantum Optics*, Cambridge University Press, 2014.
59 D. Nikogosyan, *Appl. Phys. A: Solids Surf.*, 1991, **52**, 359–368.
60 J. P. Villabona-Monsalve, O. Calderón-Losada, M. Nuñez Portela and A. Valencia, *J. Phys. Chem. A*, 2017, **121**, 7869–7875.
61 N. P. Barnes, D. J. Gettemy and R. S. Adhav, *J. Opt. Soc. Am.*, 1982, **72**, 895–898.
62 U. Schlarb and K. Betzler, *Phys. Rev. B: Condens. Matter Mater. Phys.*, 1993, **48**, 15613–15620.
63 R. Dovesi, A. Erba, R. Orlando, C. M. Zicovich-Wilson, B. Civalleri, L. Maschio, M. Rérat, S. Casassa, J. Baima, S. Salustro and B. Kirtman, *Wiley Interdiscip. Rev.: Comput. Mol. Sci.*, 2018, **8**, e1360.
64 J. Li, S. Gauza and S.-T. Wu, *J. Appl. Phys.*, 2004, **96**, 19–24.
65 C.-W. Chen, H.-C. Jau, C.-H. Lee, C.-C. Li, C.-T. Hou, C.-W. Wu, T.-H. Lin and I. C. Khoo, *Opt. Mater. Express*, 2013, **3**, 527–532.
66 N. Xie, H. Zhang, B. Liu, B. Song and J. Wu, *J. Lightwave Technol.*, 2017, **35**, 2966–2972.